Original research article

Journal of Vibration and Control
2026, Vol. 0(0) 1–19
© The Author(s) 2026
Article reuse guidelines:
sagepub.com/journals-permissions
DOI: 10.1177/10775463261420711
journals.sagepub.com/home/jvc
Sage

Modeling and TF-BPNN inverse modeling of a magnetorheological damper

Xinmiao Chen[1], Yuan Yao[1], Huajie Su[1] and Jinchuang Qiao[1]

Abstract

Rail vehicles equipped with secondary semi-active suspension can effectively improve ride quality. Magnetorheological (MR) dampers are widely used as actuators in semi-active suspensions due to their advantages such as rapid response and wide adjustment range. However, their complex nonlinear characteristics pose challenges for research and application. This paper studies modeling of a MR damper and its inverse models. For MR damper modeling, a physical model is developed that incorporates both the shear-thinning effect and viscoelastic characteristics of MR fluids by integrating the bi-plastic Bingham model and the Maxwell model. The proposed model provides greater physical interpretability and a more accurate characterization of the mechanical behavior than a widely used improved Bouc-Wen hysteresis model. This performance is validated by Hardware-in-the-loop (HIL) tests on a 3-DOF rail vehicle lateral model. The proposed model outperformed an improved Bouc-Wen model, with a lower overall RMSE (55.7 N vs 103.1 N) and a smaller average amplitude error under small-amplitude vibration conditions in the 17–18 Hz range (7.5% vs 27%). For the MR damper inverse model, a Transfer function - Back Propagation Neural Network (TF-BPNN) model was proposed to track the desired force required by semi-active control strategies. The TF component compensates for the force response lag behind the current, and the BPNN models the nonlinear relationship between force and current. HIL test results demonstrated that the TF-BPNN achieves higher R^2 values (0.857, 0.856, and 0.861 at 20°C, 31°C, and 45°C, respectively) than the Look-up table method (0.709, 0.751, and 0.786 at the same temperatures) within the critical low-frequency sway range of 1.5-2 Hz. The proposed model demonstrates high tracking accuracy and insensitivity to temperature. The validity of the developed models was experimentally verified using HIL tests, confirming their strong potential for both simulation and experimental applications.

Keywords

rail vehicles, semi-active suspension, magnetorheological damper, hardware-in-the-loop

Received: 10 July 2025; accepted: 9 January 2026

Introduction

The rapid development of rail transportation has significantly enhanced operational efficiency. However, with increasing operational mileage and higher speeds, maintaining high-level ride comfort has become a critical challenge. Traditional passive suspension systems fail to satisfy stringent comfort requirements under complex track conditions. Consequently, some researches (Zhang et al., 2022) actively explored advanced active and semi-active suspension control technologies. Semi-active suspension systems (Jin et al., 2020) offer an effective solution to this issue, enhancing rail vehicle dynamics and ride comfort while improving adaptability to complex operating environments. Extensive studies (Fu et al., 2023) confirmed their efficacy in suppressing carbody vibrations.

The core components of semi-active suspension systems are actuators and control strategies. Significant progress has been made in semi-active actuators, with representative advances including servo-valve-controlled adjustable hydraulic dampers (Ripamonti and Chiarabaglio, 2019) and magnetorheological (MR) dampers (Fu and Bruni, 2022). Although hydraulic active actuators are among the most commonly used, they impose high power requirements, which limits the practical implementation of active suspensions. Substantial research (Aboud et al., 2014) and development efforts are needed to make them commercially viable. In contrast, MR dampers have attracted widespread

[1]State Key Laboratory of Rail Transit Vehicle System, Southwest Jiaotong University, Chengdu, Peoples R China

Corresponding author:
Yuan Yao, State Key Laboratory of Rail Transit Vehicle System, Southwest Jiaotong University, 11, Chengdu 610031, Peoples R China.
Email: yyuan8848@163.com

attention due to their rapid response characteristics and wide range of damping force at low velocities (Soliman and Kaldas, 2021). Although MR dampers regarded as ideal actuators for semi-active systems, their performance potential is constrained by a contradiction. On one hand, the intrinsic MR effect introduces dynamic hysteresis, temperature sensitivity, magnetic field variations, and nonlinearities, making it exceptionally difficult to establish accurate forward models. On the other hand, achieving real-time optimal control requires solving an inverse model problem, which involves determining the command current from a desired force output and is equally challenging. Consequently, research has focused on developing refined models for MR dampers and enhancing deep reinforcement learning networks based on their dynamic characteristics to optimize control strategies. These actuators exhibit strongly nonlinear mechanical behavior, for which researchers have developed multiple mathematical models: non-Newtonian constitutive models (Bingham, bi-plastic Bingham, Herschel-Bulkley) (Gołdasz and Sapiński, 2015; Pei and Peng, 2022), hysteresis models (Bouc-wen, Tanh), and improved phenomenological models (Liu et al., 2018). Yang et al. (2024) presented a dynamic mathematical model that characterizes the system. The model incorporates a series of nonlinear springs and tanh elements, along with damping components, and is designed to predict the behavior of multi-coil MR dampers under fluid deficiency conditions. Optimization algorithms such as Particle Swarm Optimization (PSO) and Genetic Algorithms (GA) are often employed for parameter identification in these models. However, conventional parametric methods often face difficulties in parameter identification, leading to inaccurate predictions of MR damper behavior. To mitigate this, optimization techniques are implemented to improve parameter estimation in parametric approaches (Saufi et al., 2025). For instance, the predictive capability of an optimized NARX model (Liu et al., 2020) has been validated with newly measured test data. Testing and comparative results confirm that the optimized NARX network model can satisfactorily simulate the dynamic behavior of MR dampers and effectively capture the force behavior that increases with current. Although non-parametric models (Jiang et al., 2025) can achieve high accuracy, they may encounter challenges during the derivation process and typically require large amounts of high-quality training data. There are more methods (Lu et al., 2021) based on offline Look-up tables and open-loop control methods. It is also important to note (Delijani et al., 2025) that MR fluids exhibit temperature sensitivity, as their viscosity decreases with increasing temperature. This property introduces additional challenges for both forward and inverse modeling of MR dampers.

Semi-active suspension technology was first applied in the automotive field, and today, many vehicle models are equipped with MR dampers to enhance handling and comfort. Research on control algorithms has also been continuously evolving. Early developments involved classical control strategies such as Sky-Hook (SH) (Karnopp, 1996), Acceleration Driven Damping (ADD) (Savaresi et al., 2005), optimal control such as Linear Quadratic Regulator (LQR) (Hua et al., 2021), and mixed control such as SH-PDD (Liu and Zuo, 2016). For nonlinear electromechanical suspensions affected by variations in sprung mass and road input, a multi-model adaptive control scheme has been shown to significantly improve both sprung mass acceleration and tire force (Haris et al., 2016). In the context of rail vehicles, research (Wang et al., 2022) on semi-active control has primarily focused on high-speed trains. Representative approaches include second-order sliding mode control (SMC) designed via a 3-DOF vehicle model, H∞ control combined with an Adaptive Neuro-Fuzzy Inference System (ANFIS) inverse model (Zong et al., 2013), fuzzy control (Zhang et al., 2023),neural network control (Ghoniem et al., 2020) and fractional-order SH control (Zolotas and Goodall, 2018). Many of these control algorithms are implemented by using semi-active actuators to track the desired damping force. However, the output range of semi-active damping force is limited, particularly for nonlinear systems such as MR dampers. Accurate tracking of the damping force is essential to fully exploit the advantages of some control strategies. The function of calculating the control signal (current) required to achieve the desired damping force is generally referred to as the inverse model.

Hardware-in-the-loop (HIL) tests (Benninghoff et al., 2014), integrating theoretical models with physical hardware, are widely adopted in automotive applications. Liu et al. (2022) incorporated actual MR dampers, using quarter-car or multi-DOF models for semi-active suspension control simulation, and employed 17-DOF vehicle models to evaluate semi-active suspension control effectiveness. Nevertheless, Look-up table methods remain dominant for inverse models in HIL frameworks. Additionally, it was described (Yang et al., 2022) that damper transient response time and dynamic force range are crucial for semi-active suspension control efficiency.

Zhou et al. (2023) integrated semi-active suspension control with electromagnetic shunt dampers in trains, significantly reducing carbody vibration. While effective for vibration suppression, such semi-active suspension control algorithms may compromise bogie frame stability. For linear motor-driven trains, frame vibrations destabilize the motor air gap, causing fluctuating normal forces that exacerbate frame and carbody vibrations and jeopardize operational safety.

Systematic literature review reveals that current semi-active suspension control research often prioritizes control strategies, with growing emphasis on model refinement and experimental validation. Insufficient attention has been paid to two critical aspects: 1. Secondary suspension excitations primarily originate from carbody sway, bogie judder, and impact conditions. While existing MR damper models perform well at low frequencies, few studies address their behavior under combined low-frequency, high-frequency, random vibrations with impacts. 2. The inverse model based on Look-up table or open-loop control remain prevalent for desired force tracking in rail vehicle tests. Although adequate for control force tracking, damping force susceptibility to environmental variations (temperature) substantially degrades control accuracy. The main contributions of this paper are summarized as follows:

(1) A physics model for MR dampers is developed by integrating the bi-plastic Bingham model with the Maxwell model. The model possesses clear physical interpretations and accurately characterizes the mechanical characteristics.
(2) A Transfer function - Back Propagation Neural Network (TF-BPNN) inverse model is established. It shows great desired damping force-tracking ability and insensitivity to temperature capability in the critical carbody sway range of 1.5-2 Hz.
(3) A comprehensive HIL test platform is constructed, which validates the accuracy of the proposed MR damper model and confirms the superior force-tracking capability of the proposed inverse model.

MR damper model

Bi-plastic Bingham constitutive model

In an MR damper, the control input is the applied current, which energizes the built-in solenoid to generate a magnetic field. This field modulates the fluid's rheological properties, enabling controllable damping force. Previous research has typically employed the Bouc-wen model or its modifications for MR damper modeling. They have satisfactory hysteretic models within restricted excitation ranges and computational efficiency (Soliman and Kaldas, 2021). However, the identified parameters often lack physical significance and exhibit limited accuracy. This paper proposes a precise physical model for MR dampers.

Figure 1 shows the schematic layout of the single-tube MR damper model, where L_1、 L_2、 L_p, and L_g represent the lengths of the chamber 1, the chamber 2, the Annulus gap, and the high-pressure gap, respectively. P_1 and V_1 represent the pressure and volume of the chamber 1, respectively. P_2 and V_2 denote the pressure and volume of the chamber 2, respectively. P_g and V_g correspond to the pressure and volume of the high-pressure gap, respectively. A_r and A_p represent the cross-sectional areas of the piston rod and cylinder, respectively. h denotes the annular gap width.

The coefficient of volumetric elasticity, denoted by β, is defined by the relationship between pressure p and volume V.

$$\beta = -V\left(\frac{dp}{dV}\right) \tag{1}$$

The pressure variation expression for the chamber can be obtained by differentiating equation (1).

$$\frac{dp}{dt} = -\frac{\beta}{V}\left(\frac{dV}{dt}\right) \tag{2}$$

It should be noted that dV represents the volumetric change due to fluid compressibility. Given that temperature variations are neglected. The fluid in the annular gap of the piston is treated as incompressible and the cylinder is assumed rigid. Applying the principle of mass conservation, the continuity equation can be derived for the fluid flow between chamber 1 and chamber 2.

$$\dot{P}_1\left(\frac{V_1}{\beta}\right) = \dot{x}_r(A_p - A_r) - Q \tag{3}$$

$$\dot{P}_2\left(\frac{V_2}{\beta}\right) = -(\dot{x}_p - \dot{x}_g)A_P + Q \tag{4}$$

Where Q is the volume flow rate through the annular gap, and $x_r = x_p - x_t$.

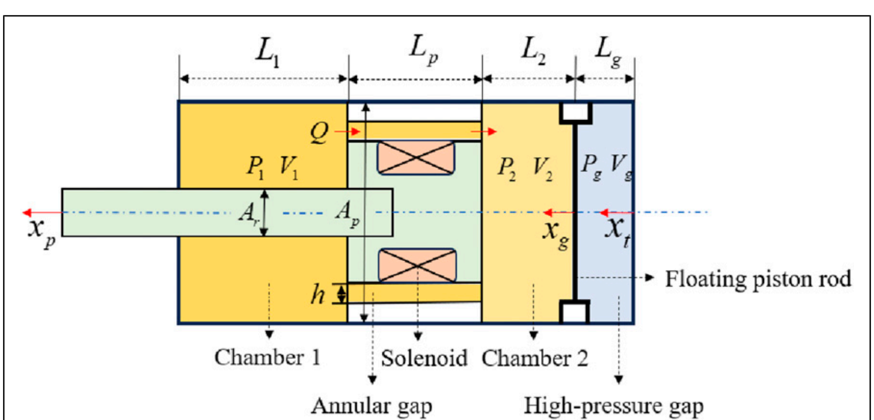

Figure 1. MR damper model schematic layout.

Assuming that the gas within the high-pressure gap undergoes adiabatic compression, let P_{g0} and V_{g0} represent the initial pressure and initial volume of the high-pressure gap, respectively. n is the adiabatic constant of the gas.

$$P_g V_g^{\ n} = P_{g0} V_{g0}^{\ n} \tag{5}$$

By differentiating equation (5) and substituting it into equation (4), the following expression can be derived:

$$\dot{P}_2\left(\frac{V_2}{\beta}\right) = -\dot{x}_p A_P + Q - \left(\frac{1}{n} V_g P_g^{\ -1} \dot{P}_g\right) \tag{6}$$

The mass of the floating piston rod and the friction between the rod and the cylinder barrel are neglected. Therefore, the pressure in the high-pressure gap is approximated as being equal to that in chamber 2. $P_2 = P_g$. The $\dot{P}_2$ is then

$$\dot{P}_2 = \beta \frac{-\dot{x}_p A_P + Q}{V_{20} + x_p A_p + V_{g0} - V_g + \frac{\beta V_g}{n P_2}} \tag{7}$$

Where V_g is defined by equation (5), and V_{20} is initial volume of the chamber 2.

Furthermore, by considering the pressure losses caused by the MR effect within the annular gap, in addition to the inertial forces arising from the equivalent mass of the fluid, the following equation can be formulated.

$$A_g \Delta p_Q + \rho L_p \dot{Q} = A_g (P_1 - P_2) \tag{8}$$

Where ρ is the fluid density and A_g is the cross-sectional area of the annular gap. As discussed in references (Gołdasz and Sapiński, 2015), to characterize the mechanical behavior of the MR damper under low-speed conditions, a mathematical model has been developed utilizing the bi-plastic Bingham model. The calculation formula for ΔP_Q is presented in reference (Gołdasz and Sapiński, 2015).

Given narrow gap dimension, low suspension velocity, and high apparent viscosity of the MR fluid, the MR fluid flow in the annular gap can be considered as laminar flow between two planar surfaces, as illustrated in Figure 2(a). The fluid flow can be assumed to have a symmetrical distribution, allowing for simplification to the flow in the lower half of the plate. Figure 2(b) depicts the relationship between shear rate and shear stress. In these figures, the u_{max} represents the maximum flow rate and the τ_{max} indicates the maximum shear stress. The bi-plastic Bingham model distinguishes pre-yield and post-yield stages. The pre-yield stage can be characterized by pre-yield viscosity μ_1 and static yield stress τ_1, while the post-yield stage is represented by post-yield viscosity u_2 and yield stress τ_2. If the local shear stress is below stress τ_1, the fluid will not flow. When the shear stress acting on the fluid is τ_1, no shear flow is generated. When the shear stress is within the range of τ_1 and τ_3, the MR fluid enters the pre-yield stage, and the shear stress rises sharply with increasing shear rate. Once the shear stress exceeds τ_3, the MR fluid transitions into the post-yield stage, where the shear stress increases slowly with shear rate. If, during the flow process, $\tau_{max} \leq \tau_3$, the bi-plastic Bingham model degenerates into the Bingham model, indicating that the MR fluid does not operate in the post-yield stage. Based on bi-

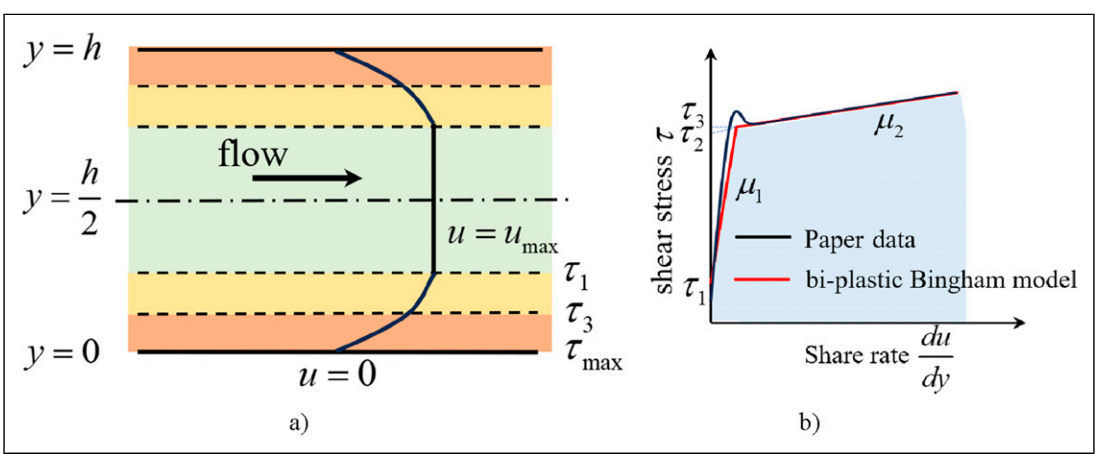

Figure 2. The bi-plastic Bingham fluid schematic layout. (a) The bi-plastic Bingham fluid in flow. (b) The bi-plastic Bingham mode and paper (Pei and Peng, 2022) data.

plastic Bingham model, the pressure losses per unit length ΔP is given by

$$\begin{cases} \Delta p^3\left(\frac{h}{2\tau_1 L\delta}\right)^3 - \Delta p^2\frac{3}{2}\left(\frac{h}{2\tau_1 L\delta}\right)^2 + \Delta p^2\left(\frac{6Q\mu}{\alpha\delta\tau_2 A_g h}\right) + \frac{1}{2} = 0 & \frac{6Q\mu}{\tau_2 wh} \le \alpha(2-3\delta+\delta^3) \\ \Delta p^3\left(\frac{h}{2\tau_1 L}\right)^3 - \Delta p^2\left(\frac{h}{2\tau_1 L}\right)^2\left(\frac{3}{2}(1-\alpha(1-\delta))\right) + \Delta p^2\left(\frac{6Q\mu}{\tau_2 A_g h}\right) + \frac{1}{2}(1-\alpha(1-\delta)) = 0 & \frac{6Q\mu}{\tau_2 wh} > \alpha(2-3\delta+\delta^3) \end{cases} \tag{9}$$

Where $\alpha = \mu_2/\mu_1$, $\delta = \tau_1/\tau_3$, $\tau_2 = \tau_3(1-\alpha(1-\delta))$. In the solutions of this equation, the root with the maximum value has physical significance and has a real solution. This root can be solved using MATLAB software, denoted as ΔP_{max}. The effective working length of the MR fluid in the annular gap is denoted as L, and thus, the pressure loss can be expressed as follows:

$$\Delta p_L = \Delta p_{\max} L \tag{10}$$

Improved model

To simulate the shear-thinning effect and avoid the discontinuous form of the bi-plastic Bingham model during calculation. The calculation method for ΔP_L is enhanced through the introduction of a tanh function. This modification addresses discontinuous transitions in shear stress during fluid flow reversal within the bi-plastic Bingham model, while simultaneously resolving viscosity discontinuities at yield stress transition regions. This functional substitution significantly improves computational efficiency and ensures improved continuity in numerical solutions. The parameter k_p is set to 10^7.

$$\Delta p_Q = \Delta p_L \times \tanh(k_p \times Q) \tag{11}$$

The mass of the piston rod and the friction between the floating piston rod and the cylinder wall are neglected. By integrating equations (3), (7), (8), and (11), the system of ordinary differential equations for chamber 1 and chamber 2 are

$$\begin{cases} \dot{P}_1 = \frac{\beta}{V_{10} - x_p(A_p - A_r)}\left[\dot{x}_r(A_p - A_r) - Q\right] \\ \dot{P}_2 = \frac{\beta(-A_P\dot{x}_p + Q)}{V_{20} + x_p A_p + V_{g0} - \left(\frac{P_{g0}V_{g0}}{P_2}\right)^{\frac{1}{n}} + \frac{\beta V_g}{nP_2}} \\ \dot{Q} = \frac{A_g(P_1 - P_2) - A_g\Delta p_Q}{\rho L_p} \end{cases} \tag{12}$$

The concept of Maxwell model is employed to improve the bi-plastic Bingham model for the MR damper in this paper. This improved model will be referred to as the BMM. A schematic diagram is presented in Figure 3, where K_{mw} and m_{mw} represent the equivalent stiffness and equivalent mass, respectively. In this model, the effects of pressure on the volumetric elastic modulus, as well as the equivalent stiffness, are considered. The MR damper exhibits the viscoelastic characteristics.

Considering the frictional force between the piston and the cylinder, denoted as F_f, and the correction force F_c. The damping force F_B can be expressed as follows, and the parameter c is set to 35:

$$F_B = (A_p - A_r)(P_1 - P_2) + F_f\tanh(c\dot{x}_r) + F_c \tag{13}$$

According to the BMM, the differential equation is:

$$m_{mw}\ddot{x}_r = (x_k - x_r)K_{mw} - F_B \tag{14}$$

Where x_k is excitation displacement.

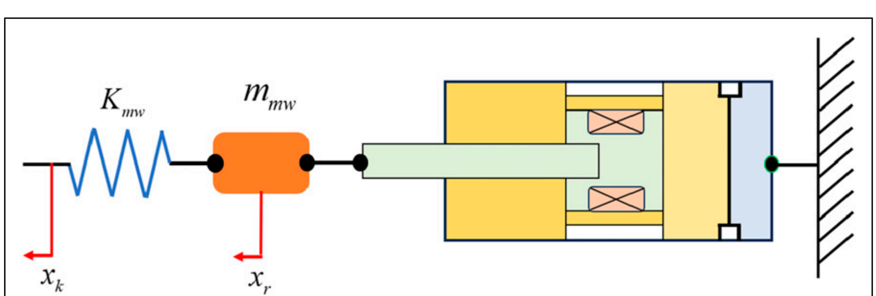

Figure 3. BMM schematic layout.

Table 1. Physical parameters of BMM.

Parameter	Description	Value
L_1	Initial chamber 1 length	32.5 mm
L_2	Initial chamber 2 length	32.5 mm
L_P	Annulus length	2×10^{-2} mm
L	Effective working length	1.75×10^{-2} mm
h	Annular gap width	1 mm
A_P	Chamber 1 cross-section area	1.32×10^{-3} m^2
A_r	Piston rod cross-sectional area	7.85×10^{-5} m^2
A_g	Annular gap cross-sectional area	9.43×10^{-5} m^2
β	Coefficient of volumetric elasticity	1.5×10^3 MPa
n	Gas adiabatic constant	1.4
m_{mw}	Equivalent mass	0.5 kg
ρ	Fluid density	2.68 g/cm^3
V_{10}	Initial chamber 1 vol	3.42×10^{-5} m^3
V_{20}	Initial chamber 2 vol	3.63×10^{-5} m^3
V_{g0}	Initial high-pressure nitrogen gap	1.95×10^{-5} m^3
P_{g0}	Initial high-pressure gap pressure	2 MPa

Parameter estimation of BMM

The physical parameters of the BMM are presented in Table. 1. The experimental tests were conducted under a frequency sweep from 1 Hz to 4 Hz with a displacement amplitude of 10 mm. The current was varied in increments of 0.1 A. According to the BMM, the identified parameters include five parameters that may be related to the current, denoted as τ_1, μ_2, α, δ, K_{mw} and two parameters related to the structural characteristics, denoted as F_f and F_c. To enhance the coherence of the manuscript, the experimental setup is comprehensively documented in the "Hardware-in-the-loop test" section.

First, two structure-related parameters, F_f and F_c, are identified, which are independent of the current. The objective function for optimization was defined as the root mean square error (RMSE) between the experimental data F_{exp}, and the simulation data F_{sim}, as given in equation (15). A genetic algorithm (GA) was employed to identify the model parameters.

$$E_{rmse} = \sqrt{\frac{\sum_{i=1}^{N} \left(F_{\exp}(i) - F_{\mathrm{mod}}(i)\right)^2}{N}} \tag{15}$$

Based on the physical significance of key parameters, the identification process begins with the parameters F_f and F_c. Here, F_f represents the friction force and F_c compensates for static equilibrium forces. Approximate constraints for these parameters can be derived under zero-current conditions. Parameters δ and α influence the flow velocity distribution across the annulus gap (Gołdasz and Sapiński, 2015). τ_1 and μ_1 are intrinsic material properties. K_{mw} affects the hysteresis behavior, with a larger value corresponding to reduced hysteresis. The constraints are specified as follows: $F_f \in$[0, 150] N, $F_c \in$[-50, 50] N, $\delta \in$[0.05, 0.2], $\alpha \in$[0.02, 0.04], $\tau_1 \in$ [0, 5]10^3 Pa, $\mu_1 \in$[0, 30] cP and $K_{mw} \in$[1, 2]10^6 N/m. The identification results are presented in Table. 2.

The values of F_f and F_c are insensitive to the current. Therefore, their average values are taken as 98.5 N and 15.2 N respectively. After setting these values, the remaining five parameters are identified, and the identification results are presented in Table. 3.

The identification results indicate that under the excitation conditions of a frequency sweep from 0.5 Hz to 4 Hz with an amplitude of 10 mm, parameters K_{mw}, δ, α, and μ_1 are insensitive to changes in current, while parameter τ_1 shows a positive correlation with the current magnitude. As illustrated in Figure 4, the fitting results obtain using a cubic polynomial demonstrate a good agreement with the experimental data.

The relationship between parameter τ_1 and the value of current I is represented by the equation. τ_1 = (-3.1539I^3 + 5.2808I^2-0.0779I + 0.0099)×10^3 kPa. These parameters K_{mw}, δ, α and μ_1 are taken as the average values from tests conducted at various current levels, 1.495 × 10^6, 0.108, 0.0356, and 14.55, respectively.

Figure 5 (a) compares the force-velocity curves of the MR damper for a frequency at approximately 2 Hz. The model effectively captures the damping force characteristics at both high and low velocities. In Figure 5 (b), the hysteresis curves of the MR damper under swept frequency excitation ranging from 1 to 3 Hz are presented, indicating its effectiveness in reflecting the damping force characteristics at both low and high velocity. Figure 6 presents the time-domain response of damping force under 1 Hz sinusoidal excitation with 10 mm amplitude, with current varying from 0A to 1A in 0.1 A increments. The results demonstrate a clear positive correlation between applied current and damping force magnitude. Notably, the BMM shows excellent agreement with experimental data, confirming that the model can accurately characterize the current-dependent sinusoidal response characteristics of the MR damper using only a single current-dependent parameter—the shear stress τ. This effective parameterization demonstrates the model's capability to capture the essential physics of MR damper behavior under harmonic excitation.

In this section, an improved MR damper model based on the bi-plastic Bingham model is established for MR dampers by incorporating the tanh function and the Maxwell model.

Table 2. Identification results of F_f and F_c.

Parameters	0 A	0.1 A	0.2 A	0.3 A	0.4 A	0.5 A	0.6 A	0.7 A	0.8 A	0.9 A	1.0 A
F_f (N)	58.1	86.5	112.5	96.2	120.2	88.3	77.7	94.5	110.5	110.5	128.5
F_c (N)	15.39	15.44	11.84	17.14	8.84	14.14	10.44	14.18	17.34	19.14	22.84

Table 3. Identification results of K_{mw} δ α τ_1 μ_1.

Parameters	0 A	0.1 A	0.2 A	0.3 A	0.4 A	0.5 A	0.6 A	0.7 A	0.8 A	0.9 A	1.0 A
K_{mw} (10^6)	1.3	1.32	1.48	1.51	1.53	1.53	1.54	1.54	1.54	1.57	1.59
δ	0.1	0.11	0.11	0.11	0.11	0.11	0.1	0.11	0.12	0.11	0.11
α	0.03	0.04	0.03	0.04	0.04	0.03	0.04	0.04	0.04	0.04	0.04
τ_1 (10^3)	0	0.06	0.17	0.40	0.60	0.91	1.16	1.47	1.70	1.95	2.04
μ_1	16.1	13.05	17.07	13.76	14.76	12.33	12.25	12.74	16.65	14.75	16.58

The proposed BMM was validated in this section using sweep frequency excitation. Subsequent validation will be conducted in Section 4 through HIL testing implemented with a half rail vehicle lateral model under Class 5 track irregularity excitation (ZHAI, 2007).

Inverse model

Figure 7 shows that the semi-active suspension control processes. Control strategy such as linear skyhook damping, LQG, LQR, and adaptive control, etc. These strategies rely on semi-active actuators to achieve desired damping forces they require. The inverse model aims to achieve optimal matching between the actual force generated by the damper and the desired force set by the control strategy. Its effectiveness is substantially challenged by the MR damper's inherent nonlinear hysteresis characteristics and pronounced environmental sensitivity. Field observations reveal significant temperature-dependent variations in damping coefficients—notably higher values during cold winters compared to hot summers—which directly impact force-tracking precision. Furthermore, the control performance is further complicated by the damper's intrinsic current-response lag and nonlinear force-velocity behavior. Current solutions like Adaptive Neuro-Fuzzy Inference Systems (ANFIS) and the Look-up table method to achieving the inverse model objectives yet still face limitations in fully compensating for the complex interplay of these dynamic factors.

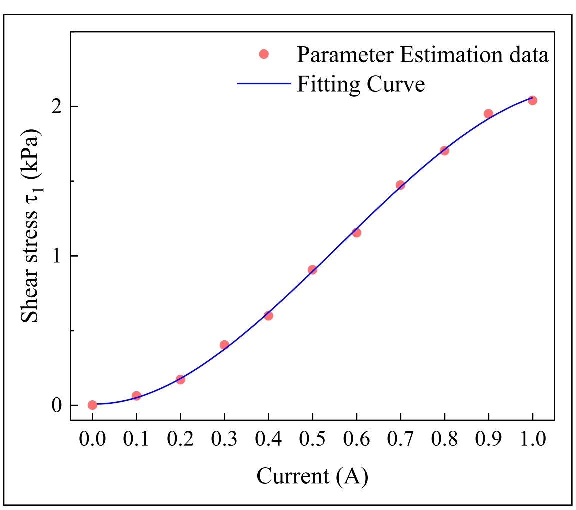

Figure 4. Relationship between τ_1 and current.

Look-up table model

Currently, Look-up table models are widely adopted in practice. These models are constructed by collecting offline experimental data that maps the damper's force-current-velocity relationship, thereby forming a three-dimensional look-up table as illustrated in Figure 8. The table data are derived from the experimental dataset described in Section 2. During operation, the desired damping force and relative velocity serve as input indices to retrieve the corresponding optimal control current value.

In practice, the exact combination of target force and velocity often does not coincide with the discrete grid points of the table. To address this, a bilinear interpolation algorithm is employed to calculate smooth, continuous target control currents based on the four nearest neighboring grid points. Some studies have proposed modified versions using damping coefficient ($C = F/v$) formulations, which fundamentally operate on the same principle. Both approaches rely on offline experimental data to establish Look-up tables for online implementation.

TF-BPNN model

Based on the preceding analysis, this study proposes a TF-BPNN model to achieve optimal matching between the desired damping force and control current. The response time of the MR damper critically influences control performance (Chen et al., 2024; Jenis et al., 2025), a factor that must be carefully considered. While prior research (Zhou et al., 2025) attempted to characterize response lag solely through current measurements, it could not fully capture the time-delay characteristics of the damping force. To systematically evaluate the current-force response dynamics, experimental testing was conducted using triangular wave displacement excitation (0.01 m/s velocity input). A 0.4 A control current was applied while the current controller adjusted output voltage based on the discrepancy between control and measured currents. All signals were recorded in real-time via the host computer. Figure 9 illustrates the system response to a step control current input, showing the measured current quickly rising and stabilizing at 0.4 A while the damping force exhibits a delayed response before settling at 500N. This hysteresis effect stems from the counter-electromotive force generated by the damper's internal solenoid during energization, which impedes magnetic field changes and consequently slows the damping force response.

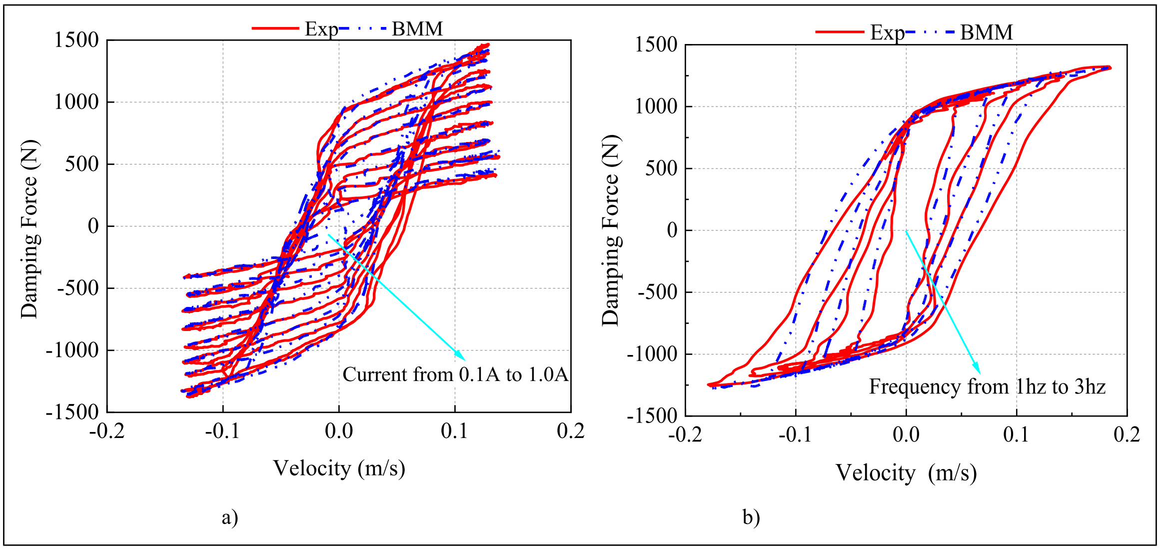

Figure 5. Comparison of curves from the tests and from numerical simulation. (a) 2Hz, 10mm. (b) from 1Hz to 3Hz, 10mm.

Figure 9 shows that when the control current is applied, the measured current quickly reaches the target value, making the damping force rise fast. Allowing some overshoot in the measured current helps get a faster damping force response, reaching about 95% of the target force in about 48 ms. The hysteresis in these processes can be modeled using an inertial element with a pure delay element.

The dynamic relationship between the measured current and the damping force is characterized by a transfer function, H(s). Notably, H(s) has a steady-state gain of 1, meaning it only shows how fast the damping force responds to measured current changes. This transfer function was identified using the System Identification Toolbox in MATLAB (2022b), with the measured current as the input and the corresponding damping force as the output. A first-order model structure with a time delay was selected for this purpose. The identified model achieved an identification accuracy of over 90%, confirming its fidelity in representing the system dynamics.

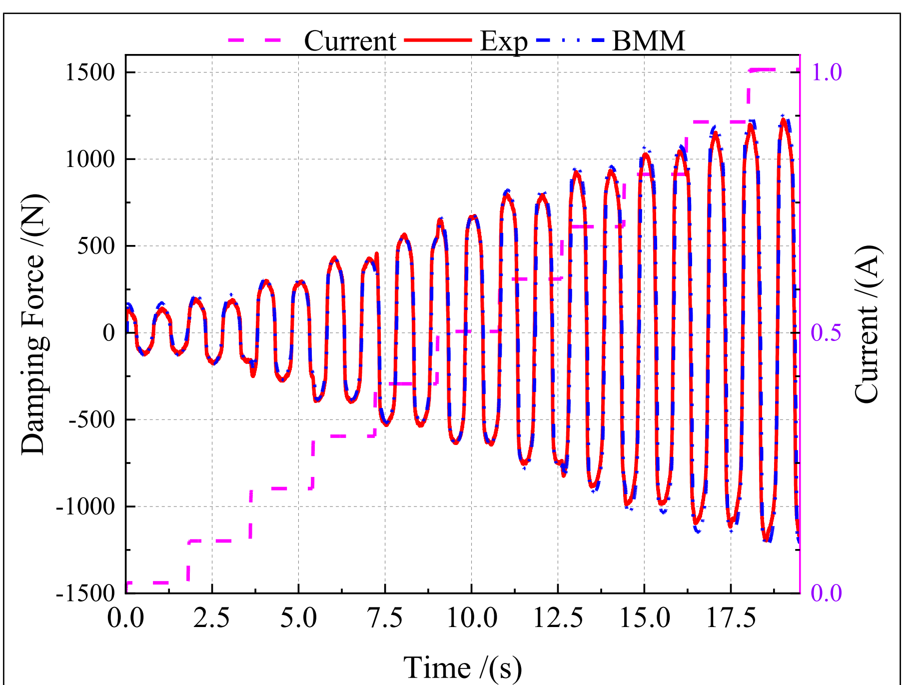

Figure 6. Comparison of curves from the tests and from numerical simulation in 1 Hz with 10 mm.

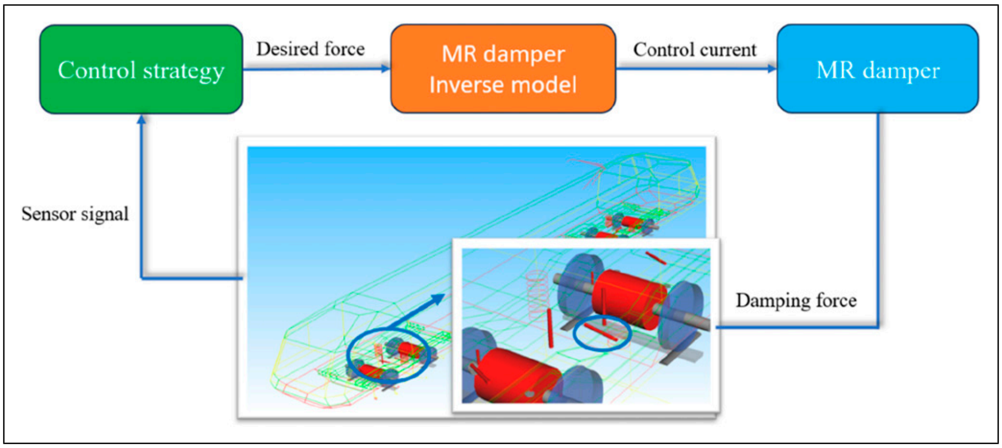

Figure 7. Semi-active suspension control process.

$$H(s) = \frac{1}{0.00956s + 1} e^{-0.005s} \tag{16}$$

The proposed TF-BPNN inverse model, shown in Figure 10 (a), integrates two components: a transfer function characterizing the dynamic damping force response to measured current, and a BPNN approximating the nonlinear current-force relationship. With three inputs (desired force, measured current, and measured force) and one output (control current), the model employs an offline-identified $H(s)$ and a BPNN whose architecture is detailed in Table. 4. Model performance was evaluated using the Mean Squared Error (MSE) defined in equation (17):

$$E_{MSE} = \frac{\sum_{i=1}^{N} \left(F_{\exp}(i) - F_{\mathrm{mod}}(i)\right)^2}{N} \tag{17}$$

Where N denotes the number of data samples, F_{exp} the measured force, and F_{mod} the predicted force.

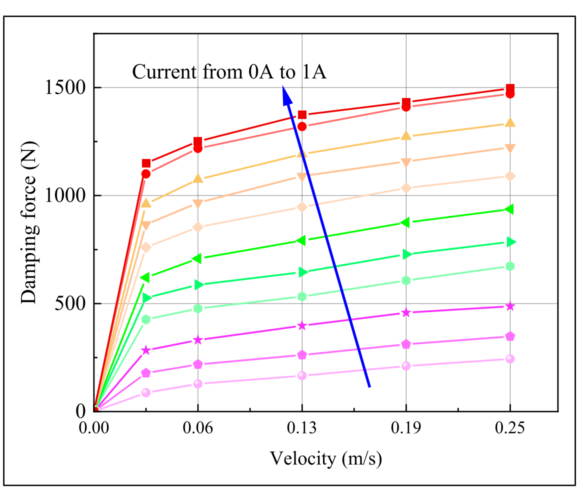

Figure 8. Three-dimensional Look-up table about Force-Current-Velocity relationship.

The primary sub-network generates NN current to track desired force. Given that desired forces frequently exceed the range of damper's control force, and neural networks exhibit unreliable extrapolation beyond training data boundaries, a protective method is implemented. Secondary sub-networks predict real-time maximum damping forces (Predictive F_{max}) and minimum damping forces (Predictive F_{min}). The system outputs NN current only when desired force lies within the $[F_{min}, F_{max}]$ range. Otherwise, it defaults to maximum or minimum current values. This cooperative framework prevents instability caused by out-of-range inputs during online operation. Based on the mathematical model of the BMM established in the previous section, dataset acquisition in Figure 10 (b) utilized 1 Hz triangular wave displacement with 0.5~30 mm amplitude. Utilizing Gaussian white noise to generate current at 0-1A with 10 Hz, collecting 2000 samples during constant-velocity excitation phases.

As shown in Figure 10 (a), a fuzzy PI control strategy is implemented to enhance the current-response speed. Thus, the response speed of the magnetorheological damping force is accelerated. This approach intentionally permits a slight current

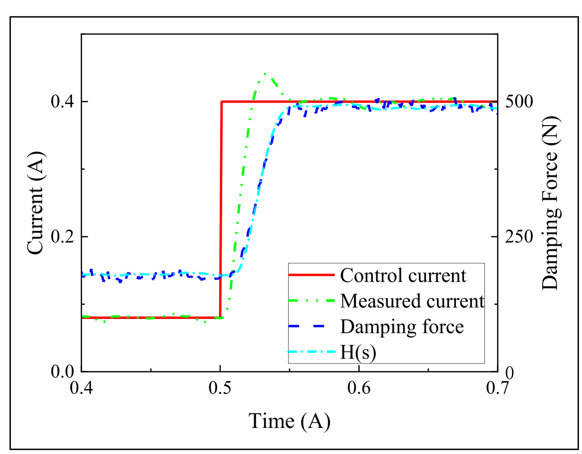

Figure 9. The responses of damping force and current.

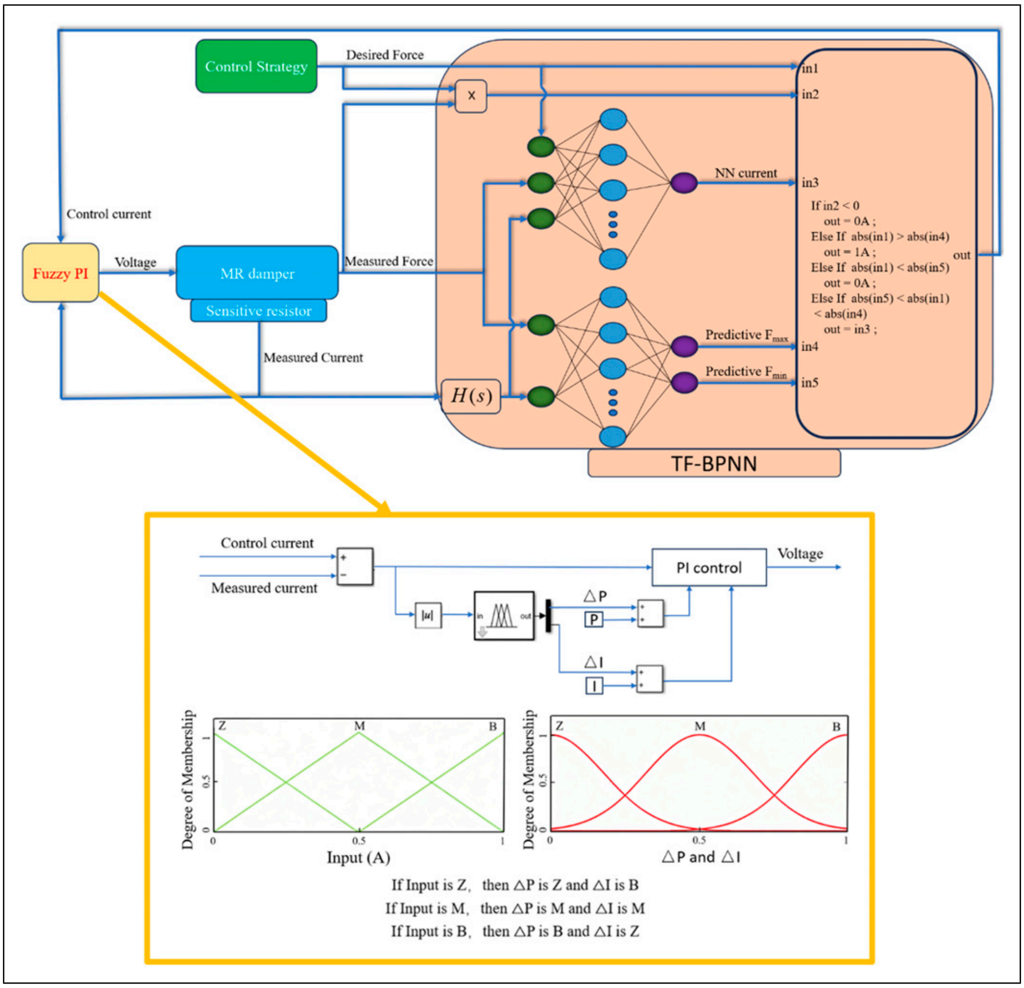

Figure 10. Schematic diagram of TF-BPNN model and training data. (a) Schematic diagram of TF-BPNN model. (b) Training data.

overshoot to accelerate system response. The controller employs larger proportional gains for larger current errors and increases integral gains while reducing proportional gains when the current error diminishes. This design achieves both fast transient response and stable performance, with the effectiveness clearly demonstrated in Figure 9.

In the fuzzy PI control structure, the final control parameters are determined by the sum of constant terms (P, I) and variable adjustments (ΔP, ΔI). The constant term P is set to 15, and I is set to 10. The input to the fuzzy logic algorithm is the absolute error between the measured current and the control current, normalized to a fundamental domain of [0, 1]. The output variables ΔP and ΔI are defined within fundamental domains of [0, 10] and [0, 10], respectively. The fuzzy system utilizes uniformly distributed triangular membership functions for inputs and uniformly distributed Gaussian membership functions for outputs. The fuzzy rule base is defined with three linguistic variables: Z (Zero), M (Mid), and B (Big). The rules are formulated as follows: IF input is Z, THEN ΔP is Z and ΔI is B; IF input is M, THEN ΔP is M and ΔI is M, IF input is B, THEN ΔP is B and ΔI is Z. The fuzzy inference system employs the Mamdani method for decision making.

Then, the control current is

$$I = \begin{cases} I_{\min} & if \quad F_m F_d < 0 \\ \left.\begin{matrix} I_{nn} & if \quad abs(F_d) \in [abs(F_{\max}), abs(F_{\min})] \\ I_{\max} & if \quad abs(F_d) > abs(F_{\max}) \\ I_{\min} & if \quad abs(F_d) < abs(F_{\min}) \end{matrix}\right\} & if \quad F_m F_d > 0 \end{cases} \tag{18}$$

Table 4. Model hyperparameters and performance results.

Hyperparameters/Results	Primary sub-network	Secondary sub-networks
Number of hidden layer neurons	Single hidden layer with 60 neurons	Single hidden layer with 120 neurons
Activation function	Sigmoid	
Training algorithm	Bayesian regularization algorithm	
Batch size for training set	1600	1600
Batch size for test set	400	400
Number of epochs	200	200
Training set MSE	0.0008 A	15.7 N (F_{max}) and 1N (F_{min})
Test set MSE	0.0011 A	26.5 N (F_{max}) and 1.5 N (F_{min})

Where I_{min}, I_{nn}, I_{max}, F_m, F_{max}, F_{min}, and F_d, represent the minimum current, NN Current, maximum current, Measured force, Predictive $\mathrm{F_{max}}$, Predictive $\mathrm{F_{min}}$ and Desired force, respectively.

Neural network models often lack interpretability and it is easy to overfit in data beyond the training data. In this study, the TF-BPNN model is divided into two distinct components: the TF-BPNN model, providing a clearer logical structure. The process of the MR damper response can be succinctly described as follows: The TF component effectively captures the dynamic lag of damping force response relative to measured current. The BPNN component models the relationship between damping force and currents. This division enhances the interpretability and understanding of the model. This model is also applicable to other semi-active actuators.

Hardware-in-the-loop test

A half rail vehicle lateral model

A half rail vehicle lateral model for rail vehicle lateral vibration is established as shown in Figure 11, where M_c, M_f, and M_w represents the carbody mass (21582 kg), the frame mass (3905 kg) and the wheel mass (1517 kg),respectively; k_s indicates the secondary lateral stiffness (3.5 × 10^5 N/m), k_p represents the primary lateral stiffness (9 × 10^6 N/m), k_{gy} represents the lateral stiffness (20 × 10^6 N/m), f_{22} represents the lateral creep coefficient (9.98 × 10^6), F_{sd} stands for the secondary lateral damper force, with y_c, y_f, y_w, and y_r respectively representing the carbody displacement, frame displacement, wheel displacement and track excitation displacement. The model differential equations are formulated as follows:

$$\begin{cases} m_c\ddot{y}_c = -k_s\left(y_c - y_f\right) + F_{sd} \\ m_f\ddot{y}_f = k_s\left(y_c - y_f\right) - F_{sd} - k_p\left(y_f - y_w\right) \\ m_w\ddot{y}_w = k_p\left(y_f - y_w\right) - 2f_{22}\dot{y}_w/v + k_{gy}\left(y_r - y_w\right) \end{cases} \tag{19}$$

The model was implemented in MATLAB/Simulink with a lateral damping force (F_{sd}) interface established, where F_{sd} is obtained through direct measurement of the actual MR damper force using force sensors, enabling real-time HIL test of the semi-active suspension system.

Experiment design

The HIL experimental setup for the 1/2 rail vehicle semi-active control system is illustrated in Figure 12 Where blue lines represent signal transmission, red boxes indicate physical components, and green boxes provide component identification. The LINKS Simulator① executes the vehicle model code and semi-active control strategy in real-time, processing the 1/2 vehicle lateral dynamics model and outputting carbody displacement signals and relative displacement between carbody and bogie to the Servo-driven system②. This system actuates the Servo motor③ to generate excitation displacements while simultaneously, the LINKS Simulator acquires and processes acceleration signals from accelerometers (Acceleration sensor④), outputting control currents to the Current controller⑤ based on the semi-active control algorithm. The current controller implements Fuzzy PI control to regulate the Driving current supplied to the MR damper⑥, which generates damping forces in response to both mechanical displacement from the servo motor and electrical input from the Current controller. A Force sensor⑦ measures these damping forces, transmitting voltage signals back to the LINKS Simulator via a Transmitter⑧, completing the HIL test that provides realistic physical quantities of the vehicle model with actual MR damper characteristics to the host computer. Additional thermocouple sensors attached to the damper surfaces enable real-time temperature monitoring.

The system was simulated with a 1 ms time step. Owing to the relatively low magnitude of the damper forces, they were scaled up by a factor of six when input to the vehicle lateral model to match the damping coefficients of actual rail vehicles. With 16-bit AD sampling precision, the HIL test meets real-time requirements while ensuring high-fidelity, repeatable test results. Unlike conventional HIL experiments that rely on idealized model-derived control signals, this configuration specifically incorporates an additional servo motor to output carbody displacement and measures vibration signals through accelerometers, ensuring all control signals originate from

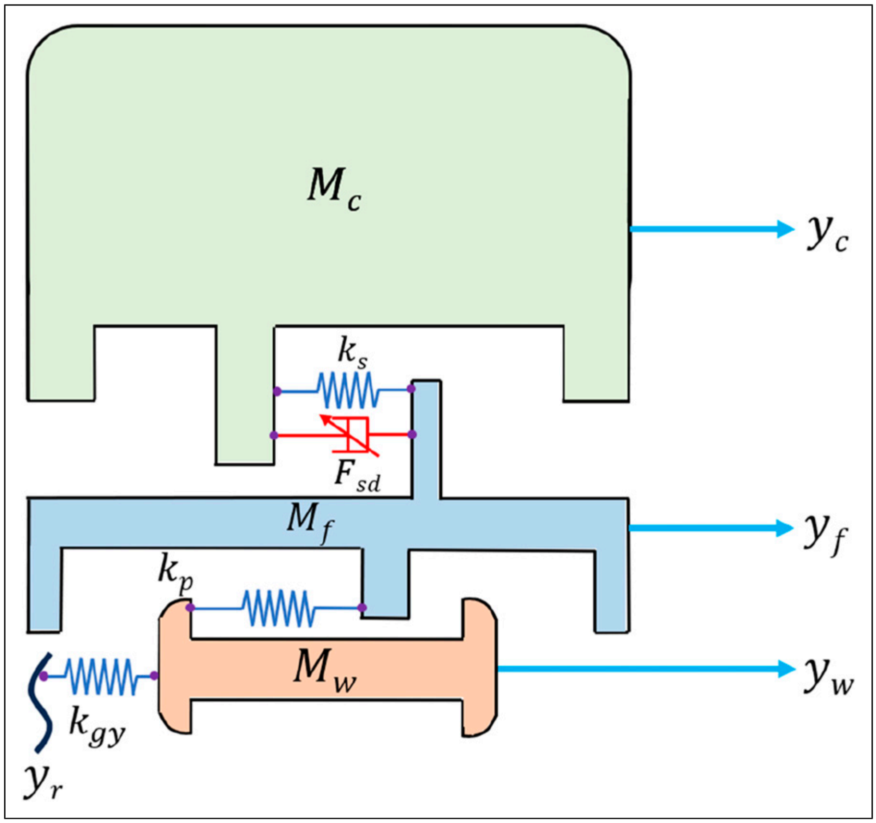

Figure 11. A half rail vehicle lateral model.

physical sensor measurements. Comparative results between measured signals and theoretical model outputs are systematically analyzed to validate system performance.

Test for MR damper model

Hysteresis models, such as the Bouc-Wen and Tanh models are widely employed in modeling magnetorheological (MR) dampers due to their computational efficiency and proven effectiveness in capturing the essential nonlinear hysteresis behavior. For comparison, this study established an improved Bouc-wen model (Liu et al., 2018) using the same experimental data from Section 2. In Figure 13, both models' force-velocity (F-V) curves were plotted with signals processed through a 15 Hz low-pass filter. The comparative results demonstrate that under these operating conditions, both models show comparable accuracy in characterizing the MR damper's mechanical properties.

Experimental validation was conducted using the HIL test platform established in Section 4.2. The rail vehicle was subjected to lateral excitation based on the US Class 5 track spectrum, filtered at 15 Hz cutoff frequency, with a vehicle speed of 150 km/h. In the HIL configuration, the measured damping forces were amplified by a factor of 6 times.

Under a constant 0.5 A excitation current applied to the MR damper, the system generated real-time relative displacement excitation while simultaneously acquiring both relative displacement signals and damping force measurements. This produced secondary lateral random displacement inputs for the half rail vehicle model. The acquired displacement signals were then applied to both the Bouc-wen model and the proposed BMM for comparative analysis. As shown in the accompanying figure, the resulting damping force outputs from both models under random displacement excitation demonstrate their respective performance characteristics.

Figure 14(a) presents a comparative time-domain analysis of damping forces from experimental data, the Bouc-wen model, and the proposed BMM. The results demonstrate that both models exhibit satisfactory dynamic characteristics when reproducing low-frequency excitation with large amplitude. However, in high-frequency excitation, small-amplitude vibration and impact conditions, compared to the Bouc-Wen model, the BMM captures these dynamic characteristics with notably greater accuracy. Model accuracy was further evaluated using the RMSE. The RMSE values are 103.1 N for the Bouc-Wen model and 55.7 N for the BMM. These results confirm that the BMM effectively captures the mechanical characteristics of the MR damper.

The spectrum in Figure 14(b) shows that both the BMM and Bouc-Wen models maintain good accuracy in the 0–5 Hz

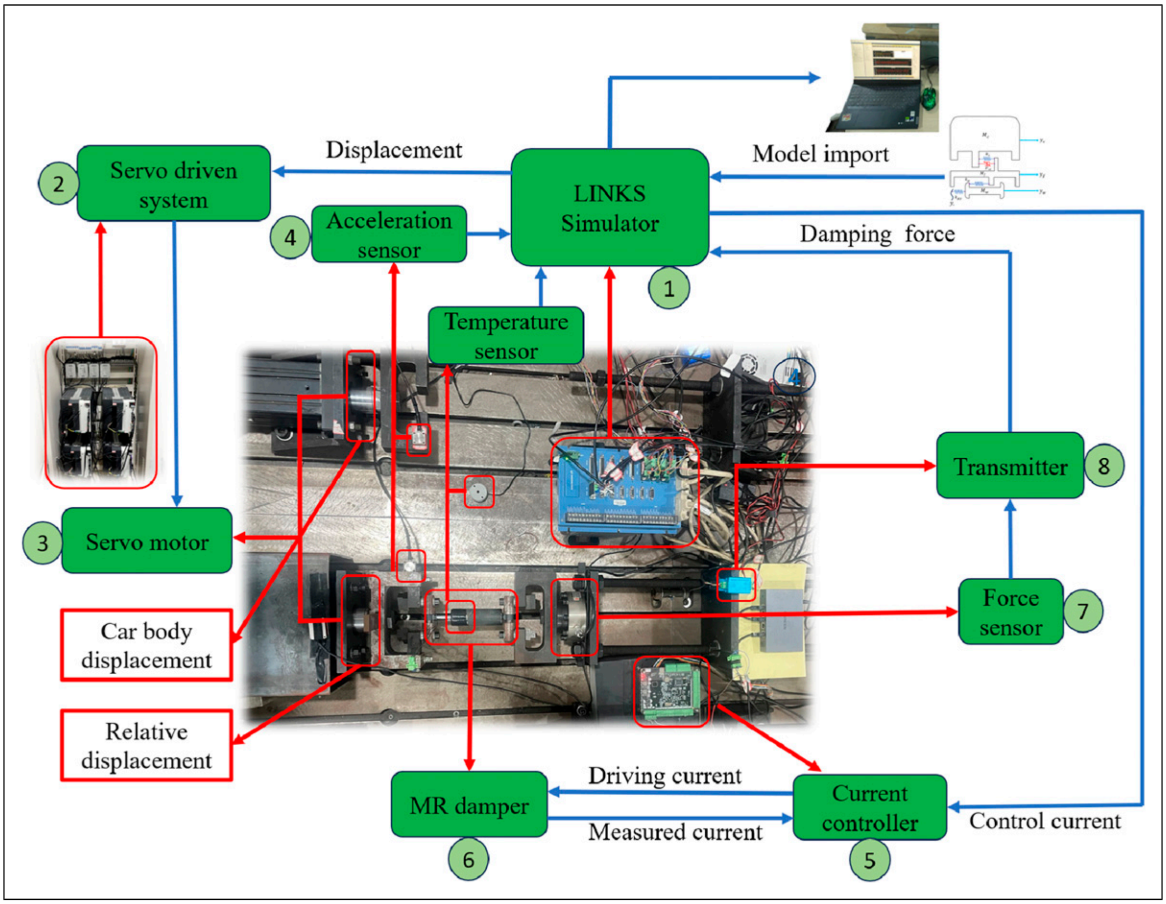

Figure 12. Schematic diagrams of hardware in the loop system.

range. As frequency increases, the BMM continues to exhibit high precision, achieving an average amplitude error of only 7.5% under small-amplitude vibration conditions in the 17–18 Hz range (7.5% vs 27%). In contrast, the accuracy of the Bouc-Wen model declines, with its average amplitude error reaching 27% in the same high-frequency range.

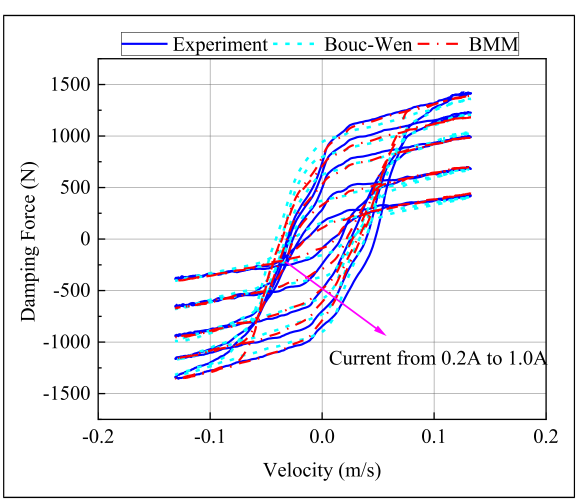

Figure 13. Comparison of curves from the tests and from numerical simulation.

This distinction carries substantial engineering implications, as bogie judder frequencies directly correspond to the secondary hunting frequency of rail vehicles-a key factor affecting operational stability. High-frequency excitation forces may induce hunting instability, particularly compromising vehicle stability during transient events like switch transitions. Although semi-active control with MR dampers demonstrates effective low-frequency vibration mitigation, its inherent time-delay characteristics pose challenges for high-frequency control requirements, causing fluctuating normal forces that exacerbate frame and carbody vibrations and jeopardize operational safety (Zhou et al., 2023).

For secondary lateral semi-active suspension systems, the robustness of control becomes paramount when addressing carbody hunting instability and bogie hunting instability. The foundation for developing such strategies lies in accurate damper modeling-the proposed BMM uniquely satisfies the dual requirements of: Low-frequency dynamics characterization (dominant carbody sway), High-frequency response fidelity (dominant bogie judder). This comprehensive modeling capability proves essential for reliable simulation of rail vehicle lateral dynamics, particularly when investigating control

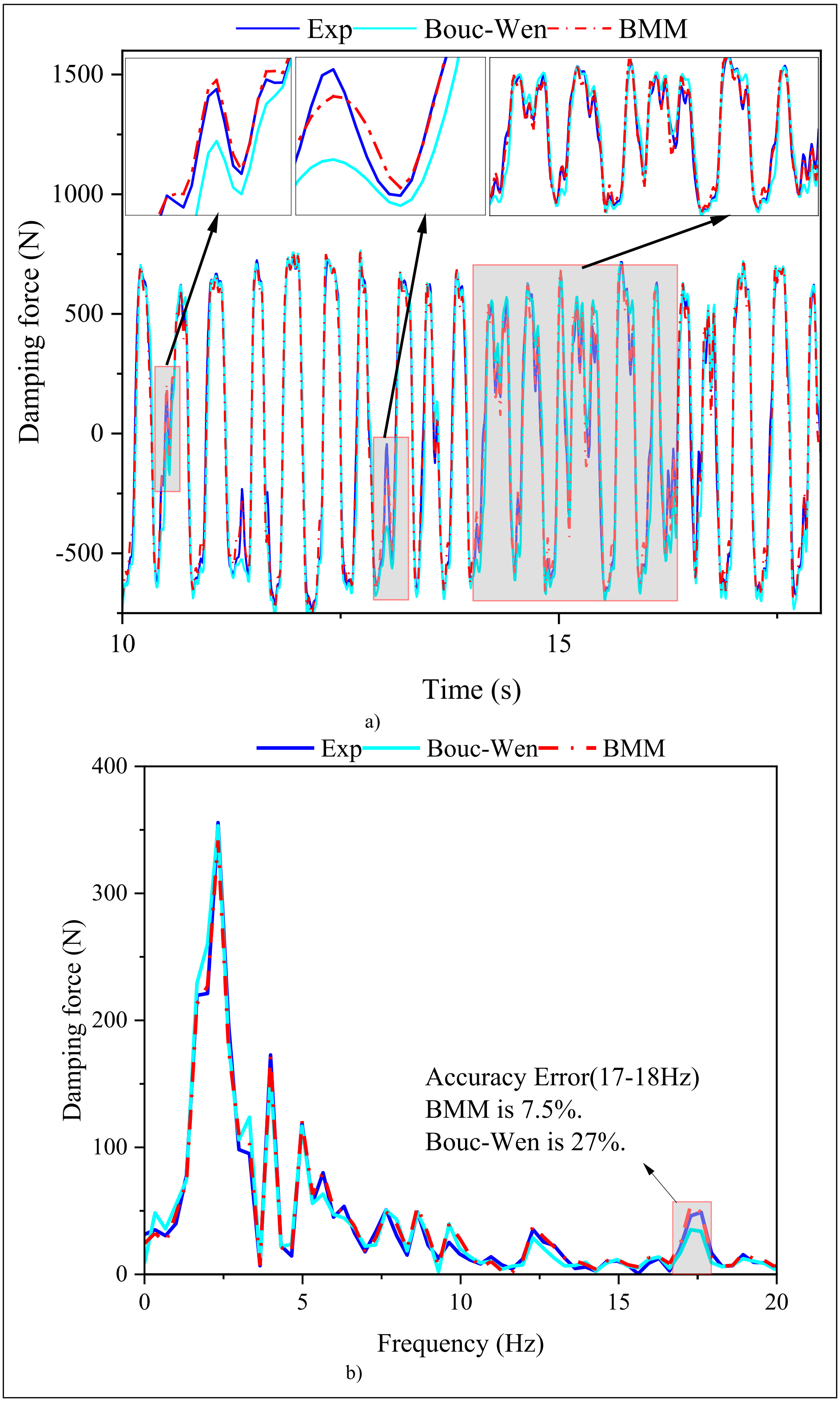

Figure 14. Comparison of curves from the tests and from numerical simulation. (a) Time domain and (b) frequency domain.

algorithms for stability-critical scenarios. The model's demonstrated accuracy across both frequency regimes establishes its superiority over conventional hysteresis models for rail-specific applications.

Test for inverse MR damper model

To compare the force-tracking performance between the Look-up table model and the proposed TF-BPNN model, experimental validation was conducted on the established HIL test platform. The system was excited by a frequency-sweep signal ranging from 1.5 Hz to 2 Hz with a constant amplitude of 4 mm. Under this operating condition, which is close to the natural vibration frequency of the carbody, the desired damping force can be tracked across the full control current range of 0 to 1 A, while maintaining a small phase difference between the desired force and actual damping force directions. This condition is conducive to comparing the ability of damping force tracking. . In the HIL test, the entire computing cycle (sensor signal sampling, control algorithm calculation, inverse model calculation) does not exceed 1 ms.

The semi-active control strategy employed a linear Sky-hook algorithm (Fu et al., 2023), where the desired damping force F_d is determined by

$$F_d = -C_{sky}\dot{y}_c \tag{20}$$

Where F_d is desired damping force, and C_{sky} is the Sky-hook damping coefficient (7×10^4 N·s/m) and $\dot{y}_c$ represents the carbody lateral velocity, emulating an "ideal wall" damping effect to suppress carbody vibrations.

The coefficient of determination, R^2, was adopted to evaluate the model's tracking performance, denoted as κ:

$$\kappa = 1 - \frac{\sum_{j=1}^{N} (F_m - F_d)^2}{\sum_{j=1}^{N} (F_m - \overline{F}_m)^2} \tag{21}$$

Where F_m and $\overline{F}_m$ are the measured damping force and its average value, respectively. N represents the total number of data points. A higher tracking capability coefficient κ indicates stronger force-tracking performance and better implementation of the semi-active control strategy.

a) displays time-domain comparisons of damping forces between measured and desired values under both Look-up table and TF-BPNN inverse models obtained through HIL tests at 20°C and 45°C. The temperature is measured using a thermocouple attached to the MR damper surface, as implemented in the temperature sensor module shown Figure 12. Overall, the TF-BPNN demonstrates superior tracking capability for the desired force compared to the Look-up table method. While the Look-up table exhibits satisfactory tracking performance at 45°C, its performance significantly deteriorates at 20°C. In contrast, the TF-BPNN maintains excellent tracking accuracy across both temperature conditions (20°C and 45°C). Notably, both methods show maximum damping forces below the desired maximum force after approximately 20 seconds, indicating operation beyond the achievable damping force range.

As shown in Table. 5, the κ values for both methods are presented at 20°C, 31°C, and 45°C. The Look-up table exhibits κ variation: 0.786 at 45°C, decreasing to 0.751 at 31°C and further to 0.709 at 20°C, representing a total variation of 14.2%. Conversely, the TF-BPNN maintains remarkable κ stability: 0.861 at 45°C, 0.856 at 31°C, and 0.857 at 20°C, with merely 0.94% variation. Although both inverse models demonstrate adequate tracking performance at 45°C, the Look-up table's effectiveness significantly declines at 20°C due to temperature-dependent variations in viscosity and shear stress of the MR fluid. It should be noted that both models were calibrated using data measured at 45°C, making them particularly suitable for characterizing damper mechanical properties at this temperature.

Figure 15(b) shows a time-domain comparison between measured and theoretically carbody velocities. Unlike conventional HIL tests that typically employ idealized control signals generated directly from simulation models, this paper utilizes actual sensor measurements for all control signal inputs, as implemented in the experimental setup shown in Figure 12. The HIL test platform employs two servo motors: one to simulate vehicle body displacement and another to reproduce suspension relative displacement. Control signals are obtained through accelerometers mounted on servo motor, with subsequent signal processing to derive the required control parameters. This approach more accurately replicates real control conditions thereby enabling more realistic evaluation of controller performance under practical operating conditions.

The inherent viscoelasticity of MR dampers introduces a phase lag in the force response relative to both displacement and velocity. A clear manifestation of this behavior can be observed. As illustrated in Figure 5, the damping force does not vanish when the velocity reaches zero but exhibits continued unloading. In contrast, Look-up table models incorrectly identify the damping force as zero at this moment, as demonstrated in Figure 8. Furthermore, as temperature increases and damping coefficient decreases, Look-up table model continues to apply current control based on the original damping coefficient, leading to performance degradation. In addition, velocity cannot be directly measured in practical applications and must be calculated through acceleration

Table 5. The κ values for look-up table and TF-BPNN at different temperatures.

	Look-up table	TF-BPNN
Temperature (°C)	κ (R^2)	
45	0.786	0.861
31	0.751	0.856
20	0.709	0.857

integration, displacement differentiation, or computational methods such as Kalman filters and predictive algorithms. These estimation techniques introduce additional lag and inaccuracies in the velocity signal.

The TF-BPNN model overcomes these limitations through two coordinated mechanisms: the transfer function component with current feedback effectively compensates for the dynamic lag between damping force response and measured current, while the BPNN incorporating both current and force feedback accurately captures the nonlinear relationship between damping force and excitation current. Even under damping variations due to change of temperature, the model dynamically adjusts the

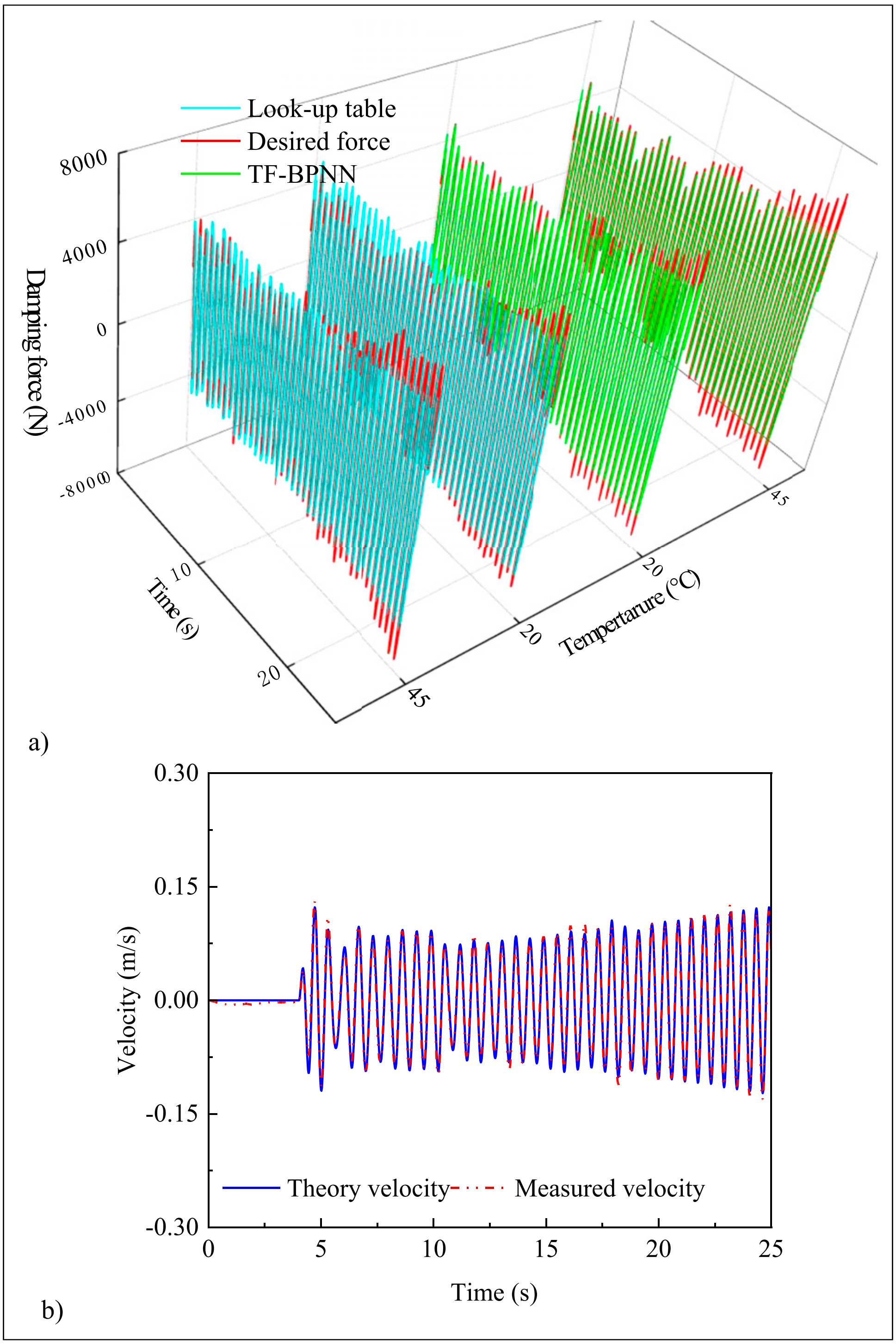

Figure 15. Comparison of curves from the tests and from numerical simulation. (a) Tracking performance comparison between TF-BPNN and Look-up table in HIL test. (b) Comparison between theoretical and measured carbody lateral velocity.

control current based on measured force and current feedback to maintain accurate tracking of the desired force.

For rail vehicles traversing extended geographical regions with substantial diurnal and seasonal temperature differentials, TF-BPNN's environmental robustness provides critical operational advantages over conventional Look-up table models in semi-active suspension systems. While the Look-up table approach provides a simple and reliable open-loop solution. However, many advanced control strategies necessitate highly accurate damping force, which typically requires the support of a high-fidelity inverse model to realize their full potential. Consequently, the choice between these modeling approaches can be determined by the specific requirements and constraints of the application at hand.

Conclusion

Models and experiments presented in this study are based on conventional magnetorheological (MR) damper materials, including magnetic particles, an oil-based carrier fluid, and functional additives. A novel MR damper model, termed the BMM, was developed and a new inverse model, designated as the TF-BPNN, was established. The following important conclusions can be drawn.

(1) The proposed BMM physical model accurately characterizes the mechanical characteristics of the MR damper. Validated on HIL test with 3-DOF rail vehicle lateral model, it demonstrated superior performance over the Bouc-Wen model, achieving a lower RMSE (55.7 N vs 103.1 N) and amplitude error (7.5% vs 27%) in the 17–18 Hz range.

(2) The TF-BPNN inverse model exhibits well desired force-tracking capability and temperature robustness, within the critical 1.5–2 Hz range. HIL tests demonstrated that the TF-BPNN achieves higher R^2 values (0.857, 0.856, and 0.861 at 20°C, 31°C, and 45°C, respectively) than the conventional Look-up table method (0.709, 0.751, and 0.786 at the same temperatures). The entire computing cycle (sensor sampling, control algorithm calculation, inverse model calculation) does not exceed 1 ms.

Based on the BMM, future work could develop a temperature-dependent physical model by incorporating the relationships between temperature, shear stress, and viscosity, or create a physics-informed neural network model. It is possible to realize the maximum potential of advanced control strategies by utilizing an accurate inverse model.

ORCID iD

Xinmiao Chen https://orcid.org/0009-0009-4378-0573

Funding

The authors disclosed receipt of the following financial support for the research, authorship, and/or publication of this article: This work was supported by the National Natural Science Foundation of China [grant numbers 52372403, U2268211], the Natural Science Foundation of Sichuan Province [grant numbers 2022NSFSC0034, 2022NSFSC1901], and the National Railway Group Science and Technology Program [grant number N2023J071].

Declaration of conflicting interests

The authors declared no potential conflicts of interest with respect to the research, authorship, and/or publication of this article.

References

Aboud WS, Haris SM and Yaacob Y (2014) Advances in the control of mechatronic suspension systems. *Journal of Zhejiang University - Science C* 15(10): 848–860.

Benninghoff H, Rems F and Boge T (2014) Development and hardware-in-the-loop test of a guidance, navigation and control system for on-orbit servicing. *Acta Astronautica* 102: 67–80.

Chen S-A, Sun Y-Z, Tong J-C, et al. (2024) Newly developed current source based shortening and modeling methods for magnetorheological damper response time. *IEEE Transactions on Intelligent Vehicles* 9(1): 417–426.

Delijani YM, Cheng S and Gherib F (2025) Operational temperature effect on the behavior of magnetorheological dampers. *Engineering Structures* 330: 119940.

Fu B and Bruni S (2022) An examination of alternative schemes for active and semi-active control of vertical car-body vibration to improve ride comfort. *Proceedings of the Institution of Mechanical Engineers - Part F: Journal of Rail and Rapid Transit* 236(4): 386–405.

Fu B, Di Gialleonardo E, Liu B, et al. (2023) Modelling, hardware-in-the-loop tests and numerical simulation of magnetorheological semi-active primary suspensions in a railway vehicle. *Vehicle System Dynamics* 62(6): 1471–1494.

Ghoniem M, Awad T and Mokhiamar O (2020) Control of a new low-cost semi-active vehicle suspension system using artificial neural networks. *Alexandria Engineering Journal* 59(5): 4013–4025.

Gołdasz J and Sapiński B (2015) Insight into magnetorheological shock absorbers.

Haris S, Aboud W and IEEE (2016) Multiple model adaptive control of a nonlinear active vehicle suspension. In: *International Conference on Advanced Mechatronic Systems (Icamechs)*. IEEE, 153–158.

Hua Y, Zhu S and Shi X (2021) High-performance semiactive secondary suspension of high-speed trains using negative stiffness and magnetorheological dampers. *Vehicle System Dynamics* 60(7): 2290–2311.

Jenis F, Michálek T, Kubík M, et al. (2025) Semi-active yaw dampers in locomotive running gear: new control algorithms and verification of their stabilising effect. *Journal of Vibration and Control* 31(13-14): 2538–2549.

Jiang M, Rui X, Yang F, et al. (2025) Non-parametric modeling of magnetorheological damper based on MEA-BP neural network. *Journal of Vibration and Control* 4: 10775463251 323321.

Jin T, Liu Z, Sun S, et al. (2020) Development and evaluation of a versatile semi-active suspension system for high-speed railway vehicles. *Mechanical Systems and Signal Processing* 135: 106338.

Karnopp D (1996) Active and semi-active vibration isolation. In: *6th Cairo-University International MDP Conference - Current Advances in Mechanical Design and Production VI (MDP-6)*. IEEE, 409–423.

Liu Y and Zuo L (2016) Mixed skyhook and Power-Driven-damper: a new low-jerk semi-active suspension control based on power flow analysis. *Journal of Dynamic Systems Measurement and Control-Transactions of the Asme* 138(8): 081009.

Liu Y, Yang S and Liao Y (2018) A new method of parameters identification for magnetorheological damper model. *Journal of Mechanical Engineering* 54(06): 62–68.

Liu Q, Chen W, Hu H, et al. (2020) An optimal NARX neural network identification model for a magnetorheological damper with force-distortion behavior. *Frontiers in Materials* 7: 10.

Liu P, Zheng M, Ning D, et al. (2022) Decoupling vibration control of a semi-active electrically interconnected suspension based on mechanical hardware-in-the-loop. *Mechanical Systems and Signal Processing* 166: 108455.

Lu H, Zhang Z, He Y, et al. (2021) Realization of desired damping characteristics based on an open-loop-controlled magnetorheological damper. *Journal of Vibration and Control* 28(23-24): 3652–3663.

Pei P and Peng Y (2022) Constitutive modeling of magnetorheological fluids: a review. *Journal of Magnetism and Magnetic Materials* 550: 169076.

Ripamonti F and Chiarabaglio A (2019) A smart solution for improving ride comfort in high-speed railway vehicles. *Journal of Vibration and Control* 25(13): 1958–1973.

Saufi MSRM, Talib MHA and Zain MZM (2025) The application of machine learning and optimisation algorithm for magnetorheological damper dynamics behaviour: a review. *Journal of Vibration Engineering & Technologies* 13(4): 231.

Savaresi S, Silani E and Bittanti S (2005) Acceleration-driven-damper (ADD): an optimal control algorithm for comfort-oriented semiactive suspensions. *Journal of Dynamic Systems Measurement and Control-Transactions of the Asme* 127(2): 218–229.

Soliman A and Kaldas M (2021) Semi-active suspension systems from research to mass-market - a review. *Journal of Low Frequency Noise, Vibration and Active Control* 40(2): 1005–1023.

Wang X, Huang D, Qin N, et al. (2022) Modeling and second-order sliding mode control for lateral vibration of high-speed train with MR dampers. *IEEE Transactions on Intelligent Transportation Systems* 23(8): 10299–10308.

Yang S, Zhao Y, Liu Y, et al. (2022) A new semi-active control strategy on lateral suspension systems of high-speed trains and its application in HIL test rig. *Vehicle System Dynamics* 61(5): 1317–1344.

Yang Y, Li Y-J, Huang X-H, et al. (2024) Force lag phenomenon in multi-coil fluid-deficient magnetorheological dampers: experimental investigation and dynamic modeling. *Smart Materials and Structures* 34(2): 025004.

Zhai W (2007) *Vehicle-Track Coupler Dynamics*. Science Press.

Zhang C, Kordestani H and Shadabfar M (2022) A combined review of vibration control strategies for high-speed trains and railway infrastructures: challenges and solutions. *Journal of Low Frequency Noise, Vibration and Active Control* 42(1): 272–291.

Zhang X, Zhou Y, Jiang C, et al. (2023) Modeling and simulation of lateral fuzzy control semi-active suspension system for high-speed trains considering time delay compensation. *Journal of Railway Science and Engineering* 20(04): 1189–1199.

Zhou X, Li H, Wang L, et al. (2023) Vertical dynamic response analysis of HTS maglev vehicle excited by a designed coreless-typed PMLSM. *Ieee Transactions on Transportation Electrification* 9(2): 3421–3433.

Zhou J, Jiang W, Huang S, et al. (2025) Shimmy vibration control of straddle-type monorail vehicle with time delay compensation based on signal influence of multisource random track surface excitation. *Mechanical Systems and Signal Processing* 230: 112620.

Zolotas AC and Goodall RM (2018) New insights from fractional order skyhook damping control for railway vehicles. *Vehicle System Dynamics* 56(11): 1658–1681.

Zong L-H, Gong X-L, Xuan S-H, et al. (2013) Semi-active H∞ control of high-speed railway vehicle suspension with magnetorheological dampers. *Vehicle System Dynamics* 51(5): 600–626.

Appendix

Abbreviation list

Abbreviation	Description
MR	Magnetorheological
HIL	Hardware-in-the-loop
RMSE	Root mean square error
TF-BPNN	Transfer function - Back Propagation Neural Network
BMM	Bi-plastic Bingham Maxwell Model
MSE	Mean square error
R^2	Coefficient of determination

Symbol list

Symbol	Unit	Description
L_1, L_2, L_P, L_g	mm	Length of Initial chamber 1, Initial chamber 2, Annulus length, high-pressure gap, respectively.
P_1, P_2, P_g	pa	Pressure of chamber 1, chamber 2, high-pressure gap, respectively.
V_1, V_2, V_g	m3	Volume of chamber 1, chamber 2, high-pressure gap, respectively.
h	mm	Annular gap width
A_P, A_r, A_g	m2	Area of chamber 1 cross-section area, Piston rod cross-sectional, Annular gap cross-sectional area, respectively.
β		Coefficient of volumetric elasticity
L	Mm	Effective working length
Q	m3/s	Volume flow rate through the annulus gap
P_{g0}	pa	Initial high-pressure gap pressure
V_{g0}, V_{20}, V_{10}	m3	Initial volume of the chamber 2, high-pressure gap, chamber 1, respectively.
n		Gas adiabatic constant
ρ	g/cm3	Fluid density
K_{mw}	N/m	Equivalent stiffness
m_{mw}	kg	Equivalent mass
δ		Static yield stress / yield stress
α		Post-yield viscosity / pre-yield viscosity
τ_1	Pa	Static yield stress
μ_1	cP	Pre-yield viscosity
I_{min}, I_{nn}, I_{max}	A	Minimum current, NN Current, maximum current,
$F_m, F_{max}, F_{min}, F_d$	N	Measured force, predictive maximum force, predictive minimum force and desired force
M_c, M_f, M_w	kg	The mass of carbody, frame and the wheel, respectively
k_s, k_p, k_{gy}	N/m	Secondary lateral stiffness, primary lateral and lateral stiffness
f_{22}		Lateral creep coefficient
F_{sd}	N	Secondary lateral damper force
y_c, y_f, y_w, y_r	mm	Displacement of carbody, frame, wheel and track excitation